RESEARCH ARTICLE

Photocurable 3D-printed PMBG/TCP biphasic scaffold mimicking vasculature for bone regeneration

Changru Zhang[1,2,3†], Ya Ren[1,2†], Weiqing Kong[2,4], Yihao Liu[2], Heyue Li[5], Han Yang[2], Bin Cai[6], Kerong Dai[1,2], Chengwei Wang[2*], Liang Tang[7*], Haoyi Niu[2*], Jinwu Wang[1,2*]

[1]Southwest JiaoTong University College of Medicine, No. 111 North 1st Section of Second Ring Road, Chengdu 610036, China

[2]Shanghai Key Laboratory of Orthopaedic Implant, Department of Orthopaedic Surgery, Shanghai Ninth People's Hospital Affiliated Shanghai Jiao Tong University School of Medicine, 639 Zhizaoju Rd, Shanghai 200011, China

[3]Institute of Translational Medicine, Shanghai JiaoTong University, No. 800 Dongchuan Road, Shanghai 200240, China

[4]Department of Spinal Surgery, The Affiliated Hospital of Qingdao University, No. 59 Haier Road, Qingdao, Shandong Province 266000, China

[5]Shanghai Seventh People's Hospital, Affiliated to Shanghai University of Traditional Chinese Medicine, Obstetrics and Gynecology, No. 358 Datong Road, Shanghai 200137, China

[6]Department of Rehabilitation Medicine, Shanghai Ninth People's Hospital, Shanghai Jiao Tong University School of Medicine, No. 500 Quxi Road, Shanghai 200011, China

[7]Department of Orthopedic Surgery, Tongren Hospital, Shanghai Jiao Tong University School of Medicine, No. 1111 XianXia Road, Shanghai 200336, China

†These authors contributed equally to this work.

*Corresponding authors:
Chengwei Wang
(wangcw_1222@163.com)

Liang Tang
(hts03@126.com)

Haoyi Niu
(haoyiniu@163.com)

Jinwu Wang
(wangjw-team@shsmu.edu.cn)

Abstract

Mesoporous bioglass (MBG) with excellent osteointegration, osteoinduction, and biodegradability is a promising material for bone regeneration. However, its clinical application is hindered by complex processing and a lack of personalization, low mechanical strength, and uncontrollable degradation rate. In this study, we developed a double-bond-functionalized photocurable mesoporous bioglass (PMBG) sol that enabled ultrafast photopolymerization within 5 s. By further integrating nanosized tricalcium phosphate (TCP) particles through three-dimensional (3D) printing technology, we fabricated personalized and highly porous PMBG/TCP biphasic scaffolds. The mechanical properties and degradation behavior of the scaffolds were regulated by varying the amount of TCP doping. *In vitro* and *in vivo* experiments verified that PMBG/TCP scaffolds slowly released SiO_4^{4-} and Ca^{2+}, forming a vascularized bone regeneration microenvironment within the fully interconnected pore channels of the scaffold. This microenvironment promoted angiogenesis and accelerated bone tissue regeneration. Overall, this work demonstrates the solution to the problem of complex processing and lack of personalization in bioglass scaffolds, and the developed PMBG/TCP biphasic scaffold is an ideal material for bone regeneration applications with broad clinical prospects.

Keywords: Photocurable mesoporous bioglass; Personalization; Bone repair; Angiogenesis

1. Introduction

The number of patients with bone defects caused by factors such as osteoporosis, bone tumors, and infections is growing rapidly, creating a huge clinical demand[1-3]. Autologous and allogeneic bone transplantation are internationally recognized gold standards, but their clinical application is greatly limited due to limited sources and immune rejection[4-6]. Regulating cell behavior with bioactive materials has become an important means of tissue regeneration[7-9]. Developing bioactive inducing materials that can regulate bone tissue regeneration and actively promote repair functions is currently a bottleneck problem that limits the clinical transformation of tissue regeneration technology[10-13]. Bioglass materials and calcium phosphate materials are highly biocompatible and absorbable, and their degradation products can provide a precise bone regeneration microenvironment for cells, making them an important direction for clinical application of bone regeneration-inducing materials[14-20]. Among them, biologically active glass materials can form an effective bond with the surrounding bone tissue, and the degradation releases various ions (Ca^{2+}, SiO_4^{4-}, PO_4^{3-}, etc.) and trace elements (Mg, Cu, Sr, Ce, etc.) to stimulate bone tissue regeneration and repair[21-25]. Additionally, mesoporous bioactive glass (MBG) possesses a highly organized pore structure, offering a significant surface area and favorable biocompatibility, which is conducive to the penetration and adsorption of biological and tissue fluids[25]. The multilevel pore structure (mesopores–micropores–macropores) provides a good environment for cell adhesion, proliferation, tissue growth, and migration, and also facilitates angiogenesis and growth[26]. These materials are widely used in orthopedics and dentistry. Despite this, there are still many characteristics that cannot meet the needs of bone tissue regeneration and defect repair, mainly including: (i) the lack of personalized preparation processes, which cannot accurately match specific bone defect structures and cannot meet the demands for high porosity and connectivity of the scaffold during bone regeneration; (ii) low mechanical strength, which cannot meet the mechanical strength requirements for large-sized implants, tissue regeneration, and defect repair; and (iii) the degradation rate does not match the tissue regeneration rate, which seriously affects tissue regeneration[25,27,28].

Currently, bioglass is mainly prepared by sol-gel method, which has advantages such as high controllability, good biocompatibility, and strong scalability[29,30]. However, the preparation process is cumbersome and time-consuming, and the production cost is high. Personalization of bone repair scaffolds cannot be achieved by further template method[31]. Three-dimensional (3D) printing technology has significant advantages in preparing artificial bones with specific shapes[28]. The challenge lies in how to prepare bioglass gel with printing ability, and related research shows that it is possible to solve this problem by grafting double bonds on polymer chains and further initiating polymerization through blue light[22]. Insufficient mechanical strength is a major bottleneck for large bone repair[17]. To address this issue, rigid powder particles are added to the biologically active gel to enhance its strength, and crosslinking groups (e.g., $-NH_2$, -COO-, etc.) are grafted onto the surface of bioglass particles to improve interfacial compatibility[12,32,33]. Adjusting the composition ratio of bioglass is the main means of regulating degradation. Furthermore, integrating phosphate tetrahedral units into the glass network as a component of the secondary network improves network connectivity and resists degradation[30]. Significant progress has been made in functionalizing bioglass to improve its processing ability, mechanical strength, and degradation behavior, which may meet clinical translational needs[34].

In this study, a photocurable mesoporous bioglass (PMBG) sol was developed by grafting a silane coupling agent (3-(trimethoxysilyl) propyl methacrylate, TMSPMA) onto the bioglass sol, and further composite with tricalcium phosphate (TCP) particles to prepare personalized, highly porous scaffolds using 3D printing technology, which were then sintered for bone defect repair. During the hydrolysis of tetraethyl orthosilicate (TEOS), TMSPMA underwent condensation reaction with the hydrolysis product silanol (Si-OH) to graft onto the bioglass sol, and the double bonds in the printing ink were crosslinked and cured under blue light (405 nm) when leaving the nozzle. The ink exhibited good printing performance and enabled precise preparation of large segment defects and complex structures. As shown in Scheme 1, the printed scaffolds were dried and sintered, and the phosphate units were integrated into the bioglass network. This study investigates the effects of regulating the content of TCP on both the mechanical properties and degradation behavior of scaffolds. Finally, the microenvironment for bone repair constructed by the degradation products of the biphasic scaffold and its relevant mechanisms for promoting vascularization and inducing stem cell osteogenic differentiation were investigated in depth. The PMBG/TCP scaffold developed in this study exhibited excellent comprehensive properties and has great potential for clinical application.

2. Experimental design and procedures

2.1. Materials

The materials used in this study include Pluronic® F-127 (EO106PO70EO106) from Sigma-Aldrich (St. Louis,
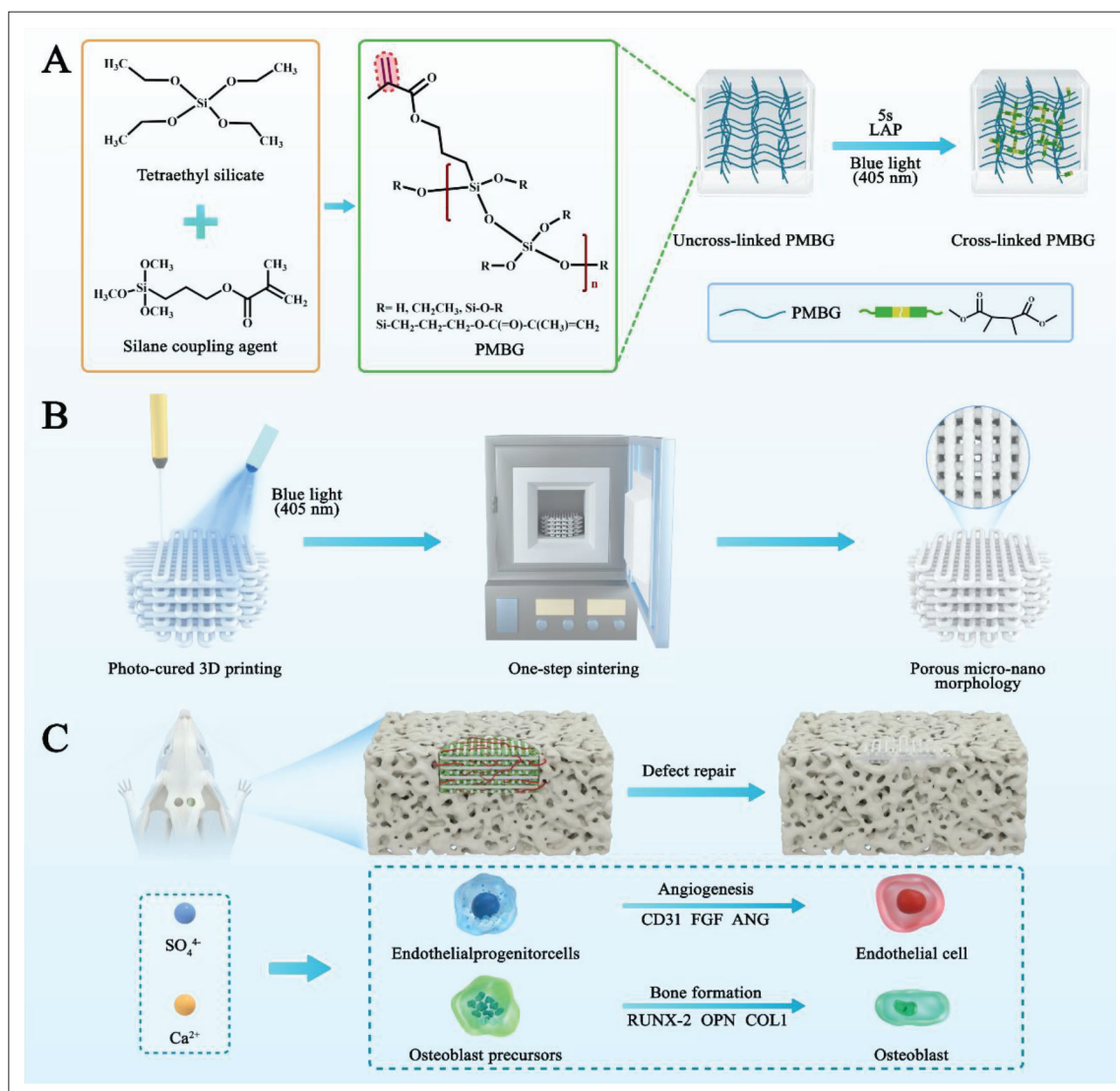
Scheme 1. (A) Schematic diagram of the synthesis process, crosslinking conditions, and principle of photocured PMBG. (B) Flowchart for the preparation of PMBG/TCP bone repair scaffold. (C) High biologically active PMBG/TCP scaffold used for bone defect repair.

MO, USA), as well as tetraethyl orthosilicate (TEOS), triethyl phosphate (TEP), hydrochloric acid (HCl), 3-(trimethoxysilyl) propyl methacrylate (TMSPMA), and glutaraldehyde from Aladdin Reagent (Shanghai) Co. (Shanghai, China). We obtained ethanol and $Ca(NO_3)_2 \cdot 4H_2O$ from Sinopharm Chemical Reagent Co., Ltd. (Shanghai, China).

2.2. Surface functionalization of bioactive glass
Photocurable MBG (PMBG) was synthesized using 3-(trimethoxysilyl) propyl methacrylate as the modifier. The synthesis process involved mixing F-127, TEOS, $Ca(NO_3)_2 \cdot 4H_2O$, HCl (0.5 M), 3-(trimethoxysilyl) propyl methacrylate, and TEP with 360 g of ethanol. The mixture was incubated for 24 h at 37°C with stirring and

subsequently suspended under vacuum at 40°C to yield PMBG gels.

2.3. Preparation of 3D-printed scaffold
Chemical precipitation was used to obtain TCP powder. First, $Ca(NO_3)_2 \cdot 4H_2O$ and $(NH_4)_2HPO_4$ were separately dissolved in ultrapure water. The solutions were continuously stirred, while the pH was maintained between 7.0 and 7.5 by adding the $Ca(NO_3)_2$ solution dropwise. After completion of the reaction, the product was centrifuged and washed four times with ultrapure water and once with ethanol to separate and purify the precipitate.

To fabricate the PMBG/TCP composite scaffold, 3D printing (using Biobuild-S, China) was employed. PMBG gels were mixed with TCP powder and LAP (at 0.5 wt%),

and the resulting slurry was continuously stirred for homogenization. The 3D-printed PMBG/TCP scaffolds were then vacuum dried at 80°C for 1 week before being calcined in a muffle furnace at 850°C, with a heating rate of 0.5°C per minute, for a duration of 6 h.

2.4. Characterization of the scaffold

The surface morphology, chemical content, and elemental distribution of the PMBG/TCP scaffolds were examined using scanning electron microscopy (SEM; GAIA3, Czechoslovakia) and energy dispersive spectroscopy (EDS; GAIA3, Czechoslovakia). Mechanical strength was measured using a universal material experiment device (AG-2000A, Japan) at a constant loading rate of 0.1 cm/min. Compressive strength was measured using $1 \times 1 \times 1\ cm^3$ cubes, and the ultimate compressive strength was determined as the stress at which the specimens shattered. Three test specimens were averaged to determine the findings for each group. To detect the possible presence of functional groups in the PMBG gels, Fourier-transform infrared (FTIR) spectroscopy and ^1H nuclear magnetic resonance (NMR) spectroscopy were conducted.

2.5. *In vitro* degradation and mineralization of the scaffold

The scaffolds were immersed in Tris-HCl buffer solution (200 μL/mg, pH = 7.4) and subjected to *in vitro* degradation experiments on a constant-temperature shaker at 37°C. The pH value was measured at specific time intervals, and the soaking solution was then collected. The calcium ion and silicate ion concentrations were measured using inductively coupled plasma emission spectrometry (ICP). Following a 35-day period, the scaffolds from each group were retrieved and analyzed for their surface mineralization morphology via SEM and EDS.

2.6. BMSC isolation and culture

Three male Sprague-Dawley rats, aged 6 weeks, were euthanized with an excessive dose of anesthesia (3% pentobarbital sodium) and subsequently submerged in 75% ethanol for 15 min. Bone marrow was extracted from the femurs and tibias of the rats using disinfected tools, and bone marrow-derived mesenchymal stem cells (BMSCs) were suspended in a culture medium consisting of α-MEM (Gibco, USA) with 10% fetal bovine serum (FBS; Gibco, USA) and 1% penicillin–streptomycin (PS) (Biosharp, China), and cells were incubated at 37°C in a carbon dioxide (CO_2) incubator for the duration of the culture period. The culture medium was replenished every 2–3 days, and the BMSCs were sub-cultured when they reached 80% confluence in the culture dish. Only cells between passages three and five were used in subsequent experiments.

2.7. Biocompatibility of the scaffold

BMSCs were seeded onto a 24-well tissue culture plate at a density of 1×10^4 cells per well and co-cultured with the double-phase scaffold. Cytotoxicity was evaluated using the CCK-8 reagent (Biomake, USA). On day 1, day 3, and day 5, 600 μL of CCK-8 reagent (CCK-8: α-MEM = 10:90) was incorporated to each well. After 2 h of incubation, 0.1 mL of the incubation supernatant was collected and analyzed using an enzyme immunoassay (EIA) reader to measure the absorbance at 450 nm. To assess cell viability after 48 h of co-culturing with the scaffold, a live/dead cell kit (YEASEN, China) was used. A fluorescence lens was used to see the stained cells after they had been stained with a mixed dye for 40 min (600× magnification).

2.8. Alkaline phosphatase staining and Alizarin red S staining

BMSCs were seeded onto the scaffold at a density of 1×10^4 cells per well in 24-well plates and allowed to adhere for 24 h. After this initial period, the cells were induced to differentiate into osteoblasts by the addition of a specific medium. The cells were stained with an alkaline phosphatase (ALP) kit (YEASEN, China) after 7 days of culture, and the optical density (OD) values were determined by enzyme labeling at 405 nm.

To observe the mineralized nodules formed by the BMSCs on the scaffolds, Alizarin red S (ARS) staining was performed. The same cell culture process was used as for the ALP staining, except that the Alizarin Red kit (Beyotime, C0138) was used for staining after 21 days of cell growth. After staining, the culture plates were treated with 10% acetic acid and incubated overnight to dissolve the dye. After 15 min of centrifugation, the supernatant was combined with a 10% ammonium hydroxide solution, and the OD value was measured using the same method as for the ALP assay.

2.9. Tube formation investigation of scaffolds

To prepare the substrate, Matrigel was applied to the surface of a 24-well plate and incubated in fresh Dulbecco's Modified Eagle Medium (DMEM) at 37°C for 1 h. A substrate was inoculated with human umbilical vein endothelial cells (HUVECs) at a density of 1×10^5 cells per well and co-cultured with the extracted fluid from each group of scaffolds for 3 and 6 h in a 5% CO_2 incubator at 37°C. The results were observed using an inverted microscope. The total tube length, number of connections, number of meshes, and mesh area within each group were further analyzed using ImageJ software.

2.10. Scratch migration assay

Scratch assay was used to further explore the impact of different scaffolds on the migration of HUVECs. HUVECs

(1 × 10⁶) were seeded in a 12-well plate. When the cell density reaches 90%, a linear scratch was created using the tip of a 200-μL pipette, and the cells were washed with phosphate-buffered saline (PBS) thrice to remove dead cells and cell debris. Then, the extract of each scaffold containing 2% FBS was added; and photos of the cells were taken at 0, 12, and 24 h after scratching.

2.11. Real-time quantitative polymerase chain reaction

The expression levels of osteogenic genes (*RUNX2*, *COL1*, *OPN*, and β-actin) and angiogenic genes (*ANG*, *FGF*, and *CD31*) were evaluated using real-time quantitative polymerase chain reaction (RT-qPCR), with *GAPDH* serving as the internal reference gene. Sterile scaffolds were co-cultured with BMSCs and HUVECs.

At a density of 10⁵ cells per well, BMSCs were seeded in 6-well dishes and induced for osteogenic differentiation by changing the medium to an osteogenic induction medium containing 10^{-8} M dexamethasone, 50 μg/mL ascorbic acid, and 10 mM β-glycerophosphate, following overnight culture in α-MEM. Genomic analysis was performed on day 7. On day 2, HUVECs were seeded in DMEM at a density of 4×10^5 cells per well in 6-well plates and subjected to genetic analysis.

Total RNA was isolated from the cells using TRIzol reagent (Sangon Biotech, China), and cDNA was synthesized from the mRNA using the Prime Script RT kit from Takara, Japan, and the SYBR Green RT-PCR kit from Biomake, according to the manufacturer's protocol. Real-time PCR was conducted on a Thermo PCR instrument. The primer sequences for each gene are provided in **Table S1** (Supplementary File).

2.12. Immunofluorescence

At a density of 2×10^4 cells/cm², BMSCs were inoculated onto the various scaffold groups in α-MEM, and they were co-cultured for 7 days. Similarly, HUVECs were co-cultured with the scaffold groups in DMEM at a density of 10⁵ cells/cm². Then, each sample was fixed with 4% paraformaldehyde for 15 min and washed three times with PBS. The samples were treated with 0.1% Triton X-100 in PBS for 5 min after being blocked in a PBS solution containing 5% bovine serum albumin (BSA) for an hour. Next, the primary antibodies anti-COL1 (1:400; Proteintech) and anti-CD31 (1:400; Abcam) were incubated with the samples overnight at 4°C. Then, the secondary antibodies were incubated for 2 h at room temperature. Finally, F-actin and 4,6-Diamino-2-Phenyl Indole (DAPI) were used to stain the cytoskeletons and nuclei, respectively. The images were observed and collected using a laser scanning confocal microscope (LSCM; LSM800, ZEISS, Germany). To determine the fluorescence intensity, three random fields of view were chosen, and the fluorescence intensity was calculated using ImageJ, a tool for image analysis.

### 2.13. Surgical procedure of animal studies *in vivo*

In order to investigate the effects of scaffold treatment on bone repair and resorption, a rat cranial defect model was used. Thirty male Sprague-Dawley rats, aged 6 weeks and weighing 250 g, were divided into three groups: control, PMBG, and PMBG/TCP. In the control group, cranial defects were created without the use of any scaffold materials.

A 2-cm incision was made along the sagittal suture after the cranium had been cleaned, disinfected, and shaved. After that, the subcutaneous muscle was divided. On both sides of the parietal bone, bony defects measuring 5 mm in diameter were made using a trephine. The scaffolds were then implanted into the bone defects at a depth of 1 mm and a diameter of 5 mm. After that, 4-0 silk sutures were used to seal the skin incision. The animals were euthanized at 6 and 12 weeks following the operation, and samples from the calvarium were obtained and fixed in formalin for 72 h. The present study was performed in compliance with the Animal Care and Experiment Committee guidelines of Shanghai Ninth People's Hospital, Shanghai Jiao Tong University School of Medicine.

2.14. Bone repair assessment *in vivo*

To evaluate the efficacy of the scaffold, the animals were sacrificed at 6 and 12 weeks after the operation, and their skulls were removed and fixed with 4% paraformaldehyde for 24 h. Micro-computed tomography (micro-CT) scans were then performed on the skull defect areas, and 3D reconstructions were created for analysis. Bone volume/total volume (BV/TV) and bone mineral density (BMD) data were obtained to assess the bone repair effect of each scaffold group.

After fixation in 4% paraformaldehyde for 7 days, the tissue samples were treated with tissue fixative two more times before being decalcified in 10% Ethylene Diamine Tetraacetie Acid (EDTA) for approximately 30 days to prepare for future histopathological analysis. Hematoxylin and eosin (H&E) as well as Masson's trichrome staining were carried out following the instructions provided by the manufacturer. The samples were air-dried, then permeabilized with 0.1% Triton X-100 for 10 min prior to immunostaining. To prevent non-specific binding, the samples were treated with 5% BSA for 1 h at room temperature. Following this, they were blocked with anti-CD31 (1:200) and anti-OCN (1:200) at 4°C. After washing with PBS, appropriate Alexa fluorescence-conjugated secondary antibodies were applied for 2 h at room
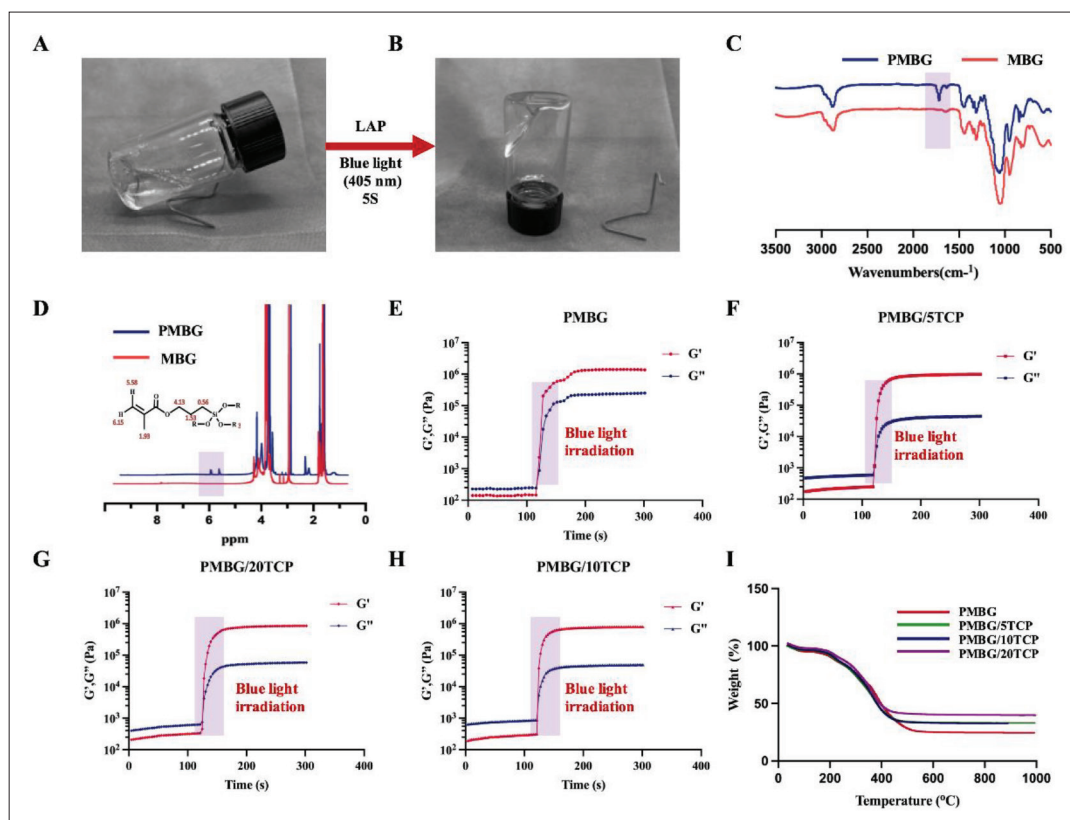
Figure 1. Ultrafast photocured mesoporous bioglasses synthesis and characterization. (A, B) The photo-crosslinking properties of PMBG. © FTIR spectra of MBG as well as PMBG. (D) ^{1}H NMR spectroscopy of MBG as well as PMBG. (E–H) PMBG, PMBG/5TCP (5% TCP), PMBG/10TCP (10% TCP), and PMBG/20TCP (20% TCP) gels photosensitive rheology. (I) Thermogravimetric analysis of PMBG scaffolds and PMBG/5TCP scaffolds, PMBG/10TCP scaffolds, and PMBG/20TCP scaffolds.

temperature. The sections were examined under LSCM after counterstaining the nuclei with DAPI.

2.15. Statistical analysis

The mean and standard deviation of each measurement were computed using descriptive statistics. To assess group differences, one-way analysis of variance (ANOVA) and Tukey's *post hoc* test were used. For statistical research, GraphPad Prism software (GraphPad Software Inc., USA) was used. A result was deemed statistically different if *$p <$ 0.05, **$p <$ 0.01, and *** $p <$ 0.001.

3. Results and discussion

3.1. PMBG gel synthesis and characterization

The precursor of PMBG was synthesized by partially replacing tetraethyl orthosilicate (TEOS) with 3-(trimethoxysilyl) propyl methacrylate (TMSPMA). PMBG exhibited rapid light-induced crosslinking properties and could be cured within 5 s (Figure 1A and B). FTIR spectra (Figure 1C) showed a peak at 1718.2 cm^{-1} for PMBG, which was absent in MBG. In addition, both sets of samples showed the vibration of Si-O-Si structure

at 1058 cm^{-1} in the FTIR spectra. This modification was further verified using ^{1}H NMR spectra. PMBG exhibited new signals at 5.58, 6.15, and 1.93 ppm, which matched the protons of the double bond of TMSPMA. This suggests that TMSPMA has been successfully incorporated into the molecules hydrolyzed or condensed from TEOS. The time-dependent rheological properties of PMBG, PMBG/5TCP (5% TCP), PMBG/10TCP (10% TCP), and PMBG/20TCP (20% TCP) were evaluated under 5% strain and 25°C using rheological tests (Figure 1E–H). Before blue light irradiation, a loss modulus (G″) value greater than the storage modulus (G′) value was observed, indicating that each group was a viscous fluid. When blue light was irradiated, G′ and G″ sharply increased, then immediately formed a crossover point, and rapidly reached a plateau, indicating that both groups underwent a light-triggered instantaneous sol-gel transition, ultimately achieving rapid and complete gelation and forming stable gels (**Videoclip S1** in Supplementary File). These results indicate that the prepared PMBG and inks doped with various proportions of TCP particles are suitable for photocuring printing.
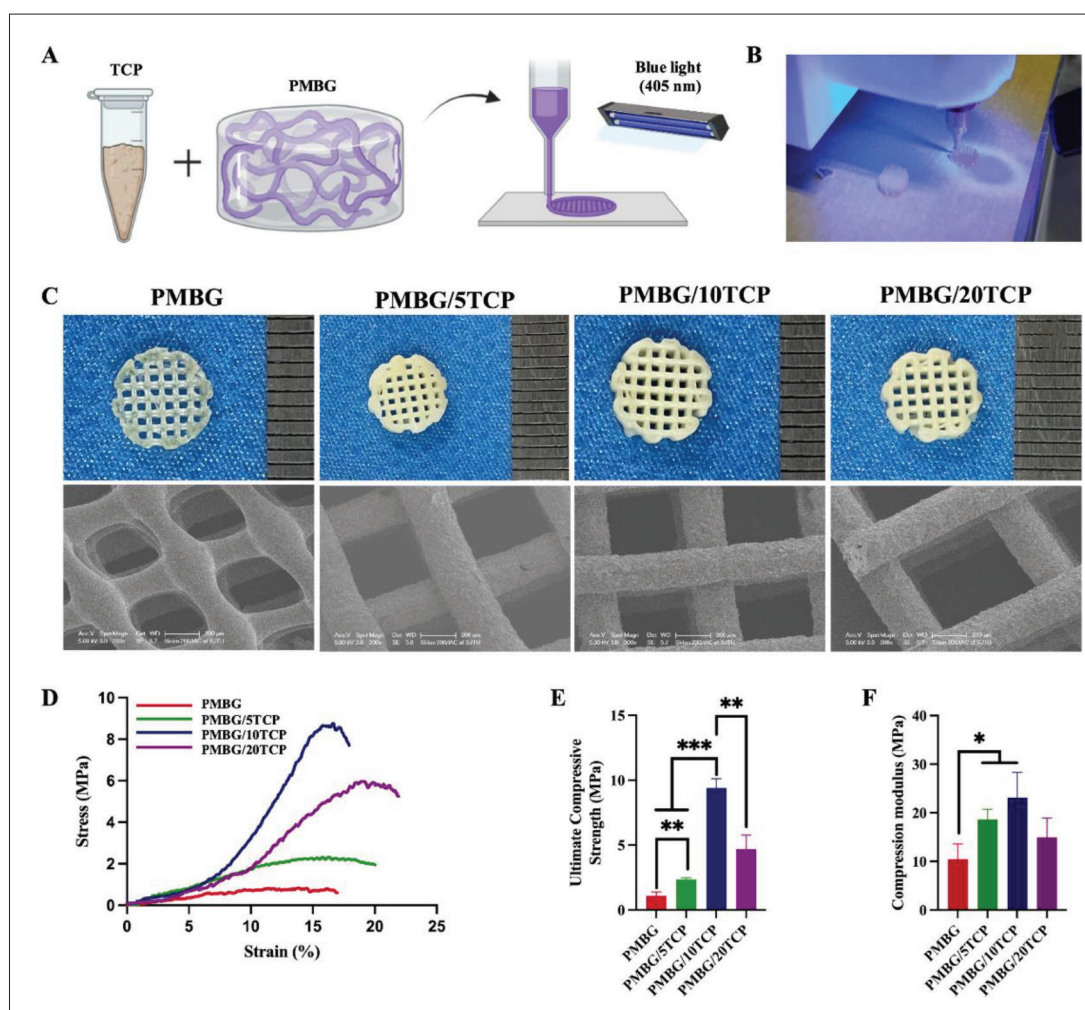
Figure 2. Printing and morphological–mechanical characterization of scaffolds. (A, B) Photocurable 3D printing diagram of PMBG scaffold and PMBG/TCP scaffold. (C) Macroscopic morphologies of PMBG scaffolds and PMBG/5TCP, PMBG/10TCP, and PMBG/20TCP scaffolds, as well as their microstructural morphologies after sintering, were observed by scanning electron microscopy for each group of scaffolds. (D) Typical stress–strain curves for each group of scaffolds. (E) Ultimate compressive strength for each group of scaffolds. (F) Compression modulus for each group of scaffolds. Created with BioRender.com.

Subsequently, thermal gravimetric analysis was performed on each group of printing ink. At 800°C, the organic framework in each scaffold was completely burned off, reaching a critical equilibrium weight loss. Therefore, we set the sintering temperature of each group of scaffolds to 850°C (Figure 1I). In order to give the scaffolds higher mechanical properties and a more regular shape after sintering, the heating rate was controlled at 0.5°C/min, and then held at the sintering temperature for 6 h. The sintered scaffolds of each group were analyzed by X-Ray Diffraction (XRD) diffraction experiment for phase analysis, and the results confirmed the characteristic peaks of the β-phase of TCP and the unoriented peak of PMBG (**Figure S1** in Supplementary File).

3.2. Preparation and physicochemical properties of scaffolds

We conducted rapid and high-fidelity photopolymerization 3D printing of PMBG and TCP particles doped with various proportions (5%, 10%, 20%) to produce scaffolds (Figure 2A and B). The surface morphology of the PMBG, PMBG/5TCP, PMBG/10TCP, and PMBG/20TCP scaffolds was observed by SEM (Figure 2C). Compared to PMBG scaffolds, TCP-doped scaffolds exhibited rougher micro-nano morphologies, and as the proportion of TCP doping increased, the number of cracks on the scaffold surface decreased, and the morphology became more regular. In addition, all scaffolds had a large interconnected porous structure with an average pore size of about 400 μm.

Transmission electron microscopy showed a nanoscale mesoporous structure with an average mesopore size of 3.833 nm (**Figures S2** and **S3** in Supplementary File). These results indicate that we successfully fabricated porous scaffolds with multiscale micro-nano structures using 3D printing.

We also evaluated the mechanical strength of the PMBG, PMBG/5TCP, PMBG/10TCP, and PMBG/20TCP scaffolds (Figure 2D). The PMBG scaffold exhibited a compressive modulus of 10.41 MPa and a compressive strength of 1.07 MPa. In comparison, scaffolds containing rigid nanoparticles (TCP) exhibit higher compressive modulus and ultimate compressive strength[34,35]. The maximum compressive strengths of PMBG/5TCP, PMBG/10TCP, and PMBG/20TCP scaffolds are 2.36, 9.4, and 4.68 MPa, respectively, and their corresponding compressive moduli are 18.61, 23.12, and 14.97 MPa, respectively (Figure 2E and F). The PMBG/10TCP scaffold exhibited the highest mechanical strength. We also tested the shrinkage rates and printing accuracies of the scaffolds after sintering. The shrinkage rates in the transverse direction of the PMBG, PMBG/5TCP, PMBG/10TCP, and PMBG/20TCP stents prepared by us are 39.89%, 37.86%, 34.90%, and 32.04%, respectively (**Figure S4A** in Supplementary File). The shrinkage rates in the sagittal plane are 40.94%, 38.07%, 34.81%, and 35.75%, respectively (**Figure S4B** in Supplementary File). The printing accuracies of the PMBG stent, PMBG/5TCP stent, PMBG/10TCP stent, and PMBG/20TCP stent are 125.3, 158.67, 193.3, and 249.3 μm, respectively (**Figure S5** in Supplementary File). Finally, using X-ray microscopy, we imaged the PMBG/10TCP scaffold and found that it had interconnected pores and a regular morphology (**Figure S6** and **Videoclip S2** in Supplementary File).

Additionally, we characterized the *in vitro* degradation of PMBG, PMBG/5TCP, PMBG/10TCP, and PMBG/20TCP scaffolds. After 35 days, the degradation rates of PMBG, PMBG/5TCP, PMBG/10TCP, and PMBG/20TCP were 39.17%, 29.53%, 24.19%, and 15.32%, respectively (Figure 3A). PMBG scaffolds degraded the fastest compared to the other scaffold groups, while the degradation rate of the scaffold decreased with increasing TCP doping ratio. This phenomenon may be attributed to the formation of more stable compounds between the phosphate ions present in the TCP particles and the calcium ions in the MBG, following the introduction of TCP into the MBG system. The resulting increase in the stability of the TCP-MBG composite could contribute to a reduction in the degradation rate of the MBG material[30,33,35], and this indicates that TCP doping can regulate the degradation rate of the scaffold, making it compatible with the rate of bone tissue regeneration. Furthermore, we measured the release rate of SiO_4^{4-} and Ca^{2+} during degradation using ICP. The results showed that SiO_4^{4-} was released slowly throughout the entire testing period, while Ca^{2+} was released suddenly in the first 2 days, followed by a slow release (Figure 3B and C). This constructed a vascularized bone regeneration microenvironment[23]. We also measured the pH value changes of the scaffold during degradation. The pH values of all scaffold groups remained between 7.1 and 7.5 (Figure 3D), indicating that the microenvironment formed by the scaffold degradation is suitable for cell growth and development. Meanwhile, after soaking the various groups of scaffolds in Tris-HCl, their surface mineralization abilities were observed using SEM and X-ray EDS after 35 days, as shown in Figure 3E. Mineral particles were detected on the surfaces of all scaffold groups. Notably, the TCP-doped scaffolds demonstrated an elevated formation of mineral particles on their surfaces, along with a corresponding increase in the accumulation of calcium and phosphorus. Importantly, this effect was found to be directly proportional to the degree of TCP doping. Therefore, considering all the advantages, PMBG/10TCP scaffolds were used for subsequent *in vitro* and *in vivo* experiments.

3.3. Biocompatibility testing of the scaffold

To assess scaffold biocompatibility, a CCK-8 cell viability assay was conducted to evaluate cell proliferation on each scaffold. As shown in Figure 4A, the proliferation behavior of MSCs co-cultured with the scaffolds in each group increased from day 1 to day 7. However, compared to the control group, the proliferation rate of cells on the PMBG and PMBG/TCP scaffolds slightly decreased. This may be due to the effect of excessive calcium ion release in the first few days, which could have an impact on cell proliferation[36]. To further validate the reliability of the CCK-8 results, a live/dead assay was conducted, as shown in Figure 4B, where green indicates live cells and red indicates dead cells. In the co-culture of cells with the PMBG and PMBG/TCP scaffolds for 48 h, there were very few red fluorescent cells observed in all groups, indicating that each scaffold possessed good biocompatibility.

3.4. Osteogenic differentiation of cells on scaffolds

An experiment was conducted using ARS staining and ALP staining to assess the promotion effects of different scaffolds on *in vitro* osteogenesis of BMSCs. ALP staining was performed on the 7th day, as ALP is a marker enzyme for early mature osteoblasts (Figure 4C). According to the study's findings, the area of ALP staining was greater in the group treated with the PMBG scaffold compared to the control group. Additionally, the group treated with the PMBG/TCP scaffold showed the largest area of ALP staining compared to the other two groups. This was
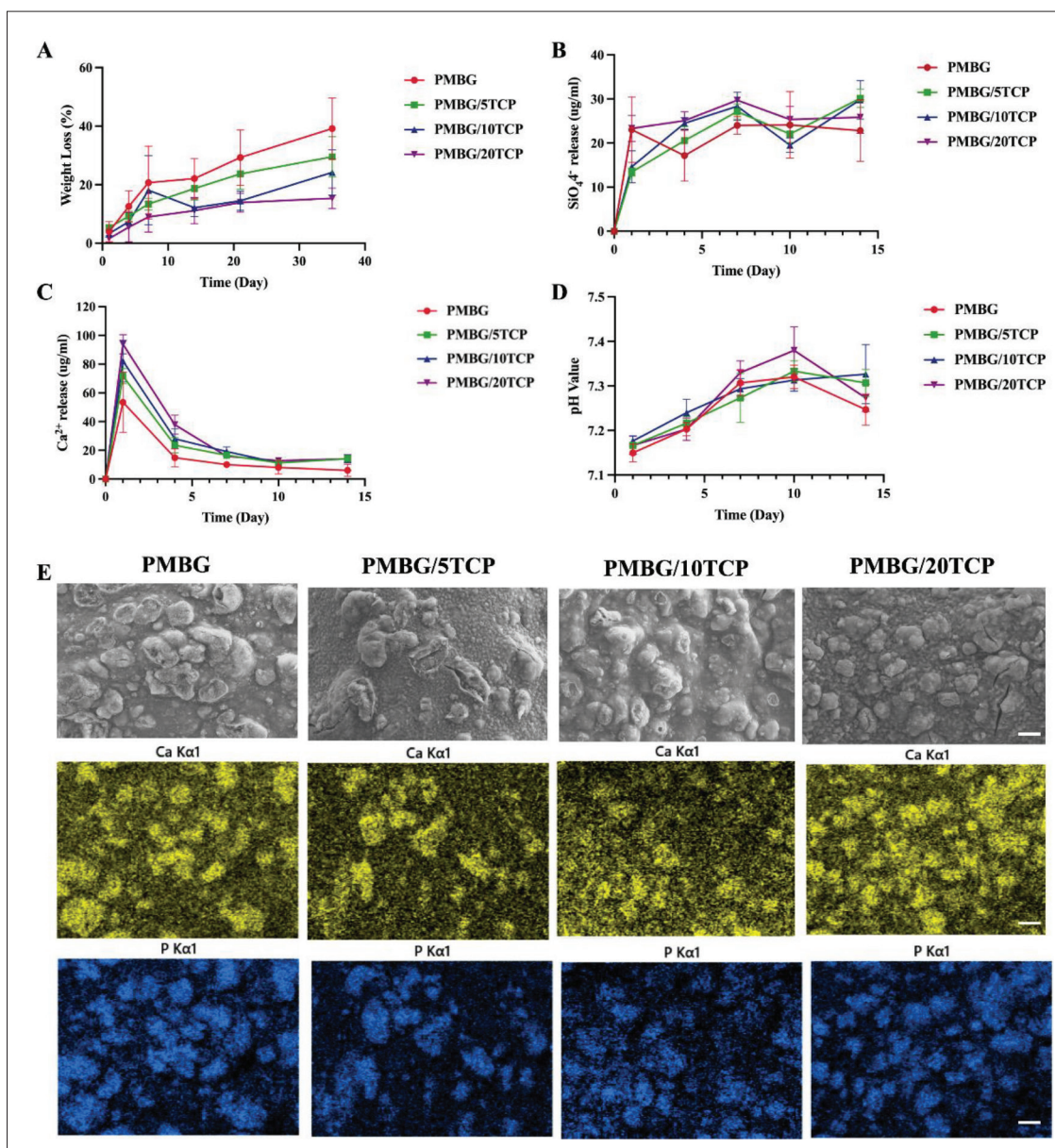
Figure 3. *In vitro* degradation and surface mineralization of each scaffold group. (A) Degradation curves of each scaffold group. Release curves of (B) SiO4^{4-} and (C) Ca^{2+}. (D) pH value of each scaffold group. (E) After 35 days of degradation experiments, the surface mineralization of each scaffold group was observed using SEM and EDS. Yellow represents calcium elements; blue represents phosphorus elements; scale bar = 10 μm.

also reflected in the quantitative analysis of ALP activity (Figure 4D). The enhanced ALP activity of the PMBG/TCP scaffold group was attributed to its release of more calcium ions. ARS staining was also conducted *in vitro* to evaluate the late-stage mineralization ability of BMSCs on different scaffolds. After 14 days of induction, the PMBG scaffold group had more mineralized nodules than the control group, and similarly, the PMBG/TCP scaffold group had even more mineralized nodules (Figure 4E). The quantitative results also demonstrated that the PMBG/TCP scaffold had the highest mineral deposition (Figure 4F).

All of the above results indicate that the PMBG/TCP scaffold possesses superior abilities to promote osteogenic differentiation.

To further elucidate the effect of PMBG/TCP scaffold on osteodifferentiation, several key target genes and proteins involved in bone formation were investigated after 7 days of co-culture of BMSCs with the different scaffolds. Immunofluorescence results indicated that the PMBG group promoted the expression of COL1 compared to the control group, while the expression level of COL1 in the
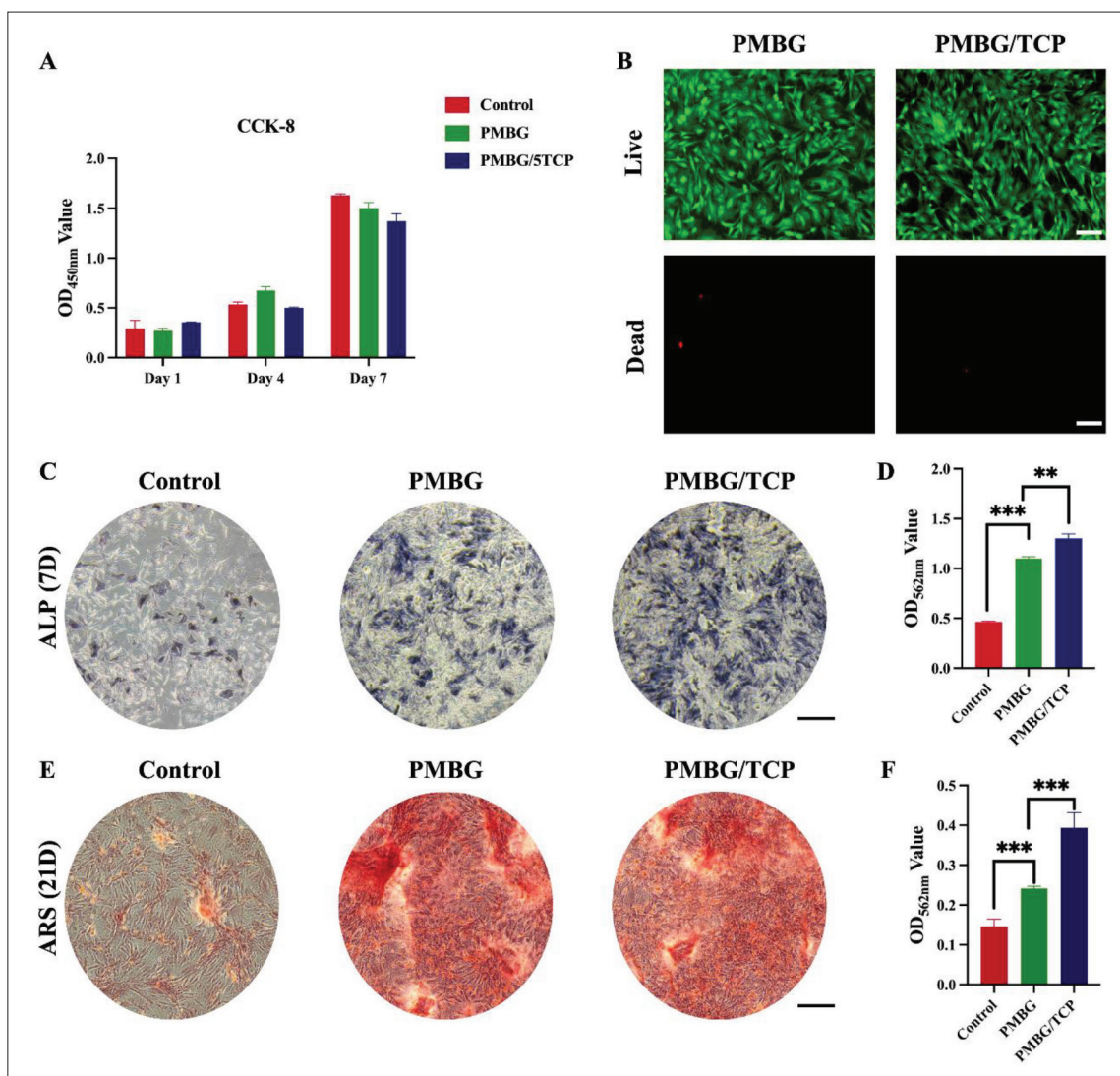
Figure 4. Biocompatibility and *in vitro* osteogenic capability of various types of prepared scaffolds. (A) Biocompatibility of BMSCs in each group, as assessed by the CCK-8 method, after 1, 4, and 7 days of culture. (B) Live/dead staining images of each group of scaffolds. (C) After 7 days of culture, cells were stained using alkaline phosphatase (ALP) staining. (D) ALP activity of cells cultured for 7 days. (E) On day 21, Alizarin red S was used to stain the cells (ARS staining). (F) Quantification of cell mineralization on day 21. Scale bar = 200 μm.

PMBG/TCP group was significantly higher than that in the other two groups (Figure 5A and B), which is consistent with the transcriptional gene expression of *RUNX2*, *OPN*, and *COL1* (Figure 5C–E). Therefore, these results demonstrate that the PMBG/TCP scaffold promotes the expression of genes and proteins related to bone formation, which in turn promotes the differentiation of BMSCs toward the osteogenic direction.

3.5. *In vitro* investigation of angiogenesis capacity on scaffolds

Due to the rich vascularization in bone tissue, the regeneration of bone tissue depends on the supply of nutrients and oxygen from blood vessels[37]. The ability

of a scaffold to promote bone tissue regeneration also depends, to some extent, on its ability to promote blood vessel formation. In this section, we also investigated the effect of PMBG/TCP scaffolds on angiogenic ability. During angiogenesis, endothelial cells need to migrate to the site of injury or ischemia and form lumens to promote the formation of new blood vessels[38,39]. Therefore, we first investigated the impact of PMBG/TCP scaffolds on the migration of HUVECs. As shown in Figure 6A and B, after co-culturing with the extract of each scaffold for 12 h, the migration rate of the PMBG scaffold group was 34.7%, the PMBG/TCP scaffold group was 42.6%, both higher than the control group's migration rate of 34.7%, with the trend becoming more apparent after 24 h. The results showed
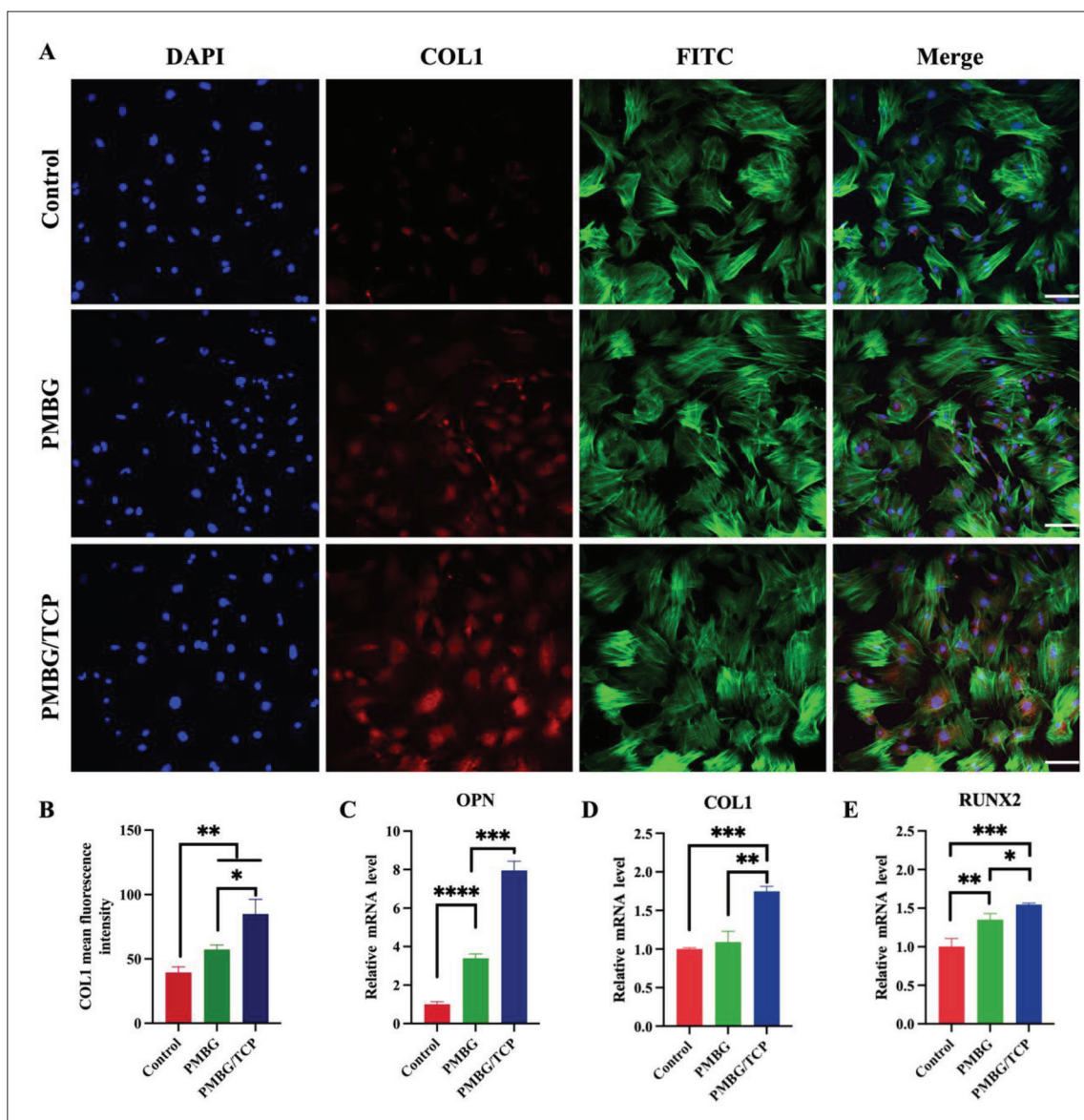
Figure 5. Effects of prepared scaffolds on osteogenic differentiation. (A, B) Immunofluorescence confocal images and quantitative analysis of the osteogenic markers COL1 (scale bar =100 μm). Osteogenic gene expression of (C) *OPN*, (D) *COL1*, and (E) *RUNX2*.

that both PMBG and PMBG/TCP scaffolds could promote HUVEC migration, with the PMBG/TCP scaffold group having the strongest migration-promoting effect. Based on the tube formation experiment results presented in Figure 6C, it was observed that the PMBG/TCP scaffold group had a higher degree of tube formation with HUVECs compared to the PMBG scaffold group and the control group at the designated time point. After using Image J to calculate the results of the tube formation experiment, we found that the various parameters calculated for the PMBG/TCP scaffold group were all higher than those for the control group and the PMBG scaffold group, and all showed a trend of increasing over time (Figure 6D and E).

Furthermore, we also explored the ability of PMBG/TCP scaffolds to promote angiogenesis at the transcriptional and protein expression levels. After co-culturing each scaffold with HUVECs for 2 days, immunofluorescence experiments were performed to detect CD31 expression. As shown in Figure 7A, HUVECs in the PMBG/TCP scaffold group expressed more CD31 (green fluorescence), and in the fluorescence quantification, the PMBG/TCP scaffold group also showed the best ability to promote CD31 expression (Figure 7B). Real-time PCR experiments were performed to detect the ability of each scaffold to promote angiogenesis at the gene transcription level. The study findings revealed that the PMBG/TCP scaffold
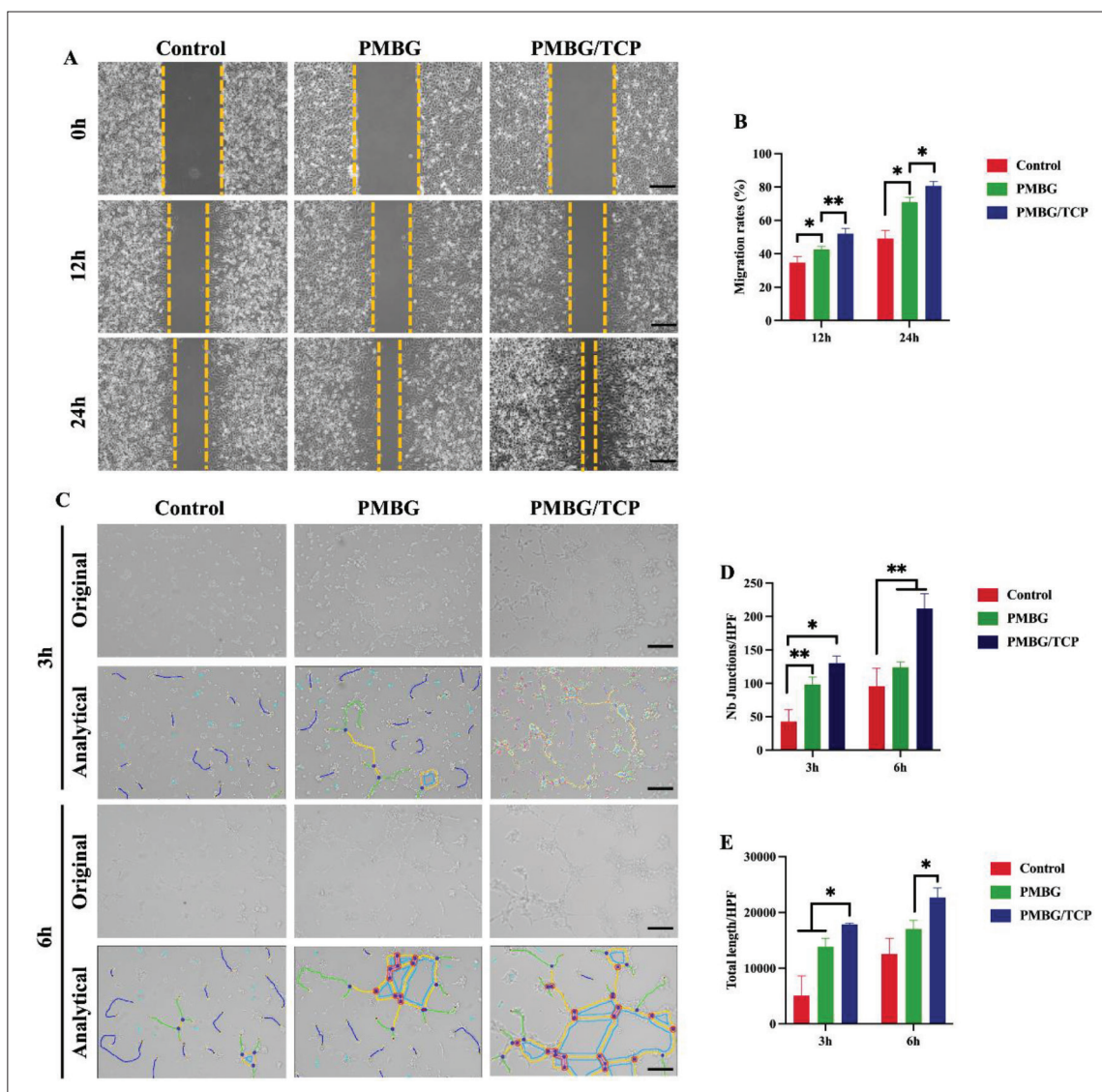
Figure 6. Capability of prepared scaffolds to promote migration and tube formation of HUVECs. (A) After co-culturing various groups of scaffolds with cells for 12 and 24 h, cell migration images were observed. (B) Analysis of cell migration rate using ImageJ. (C) Formation of endothelial network by HUVECs after 3 and 6 h of cell culture. (D, E) The number of junctions (D) and total length (E) per high power field (HPF) were analyzed. Scale bar =200 μm.

group was more effective in promoting the expression of *ANG*, *FGF*, and *CD31* genes, compared to both the control group and the PMBG scaffold group (Figure 7C–E). All of these results indicate that PMBG/TCP has the ability to promote angiogenesis and can be used for vascularized bone regeneration.

3.6. *In vivo* effects of scaffold on bone tissue regeneration

A rat calvarial defect model was used to evaluate the ability of PMBG/TCP scaffolds fabricated by photopolymerization-assisted 3D printing to promote vascularized bone regeneration. The cylindrical scaffolds

implanted during surgery fit well with the defect site, demonstrating their personalized fabrication. Throughout the entire animal experiment period, no infections or deaths were observed. Rats were euthanized at 6 and 12 weeks after surgery, and X-ray analysis was performed on the skulls. As shown in Figure 8A and B, the PMBG/TCP scaffold group significantly enhanced new bone formation and growth compared to the other two groups, while the control group exhibited the least bone regeneration. In addition, quantitative micro-CT analysis showed that the BMD and BV/TV in the control group were significantly lower than those in the PMBG scaffold group and the PMBG/TCP scaffold group at all predetermined time
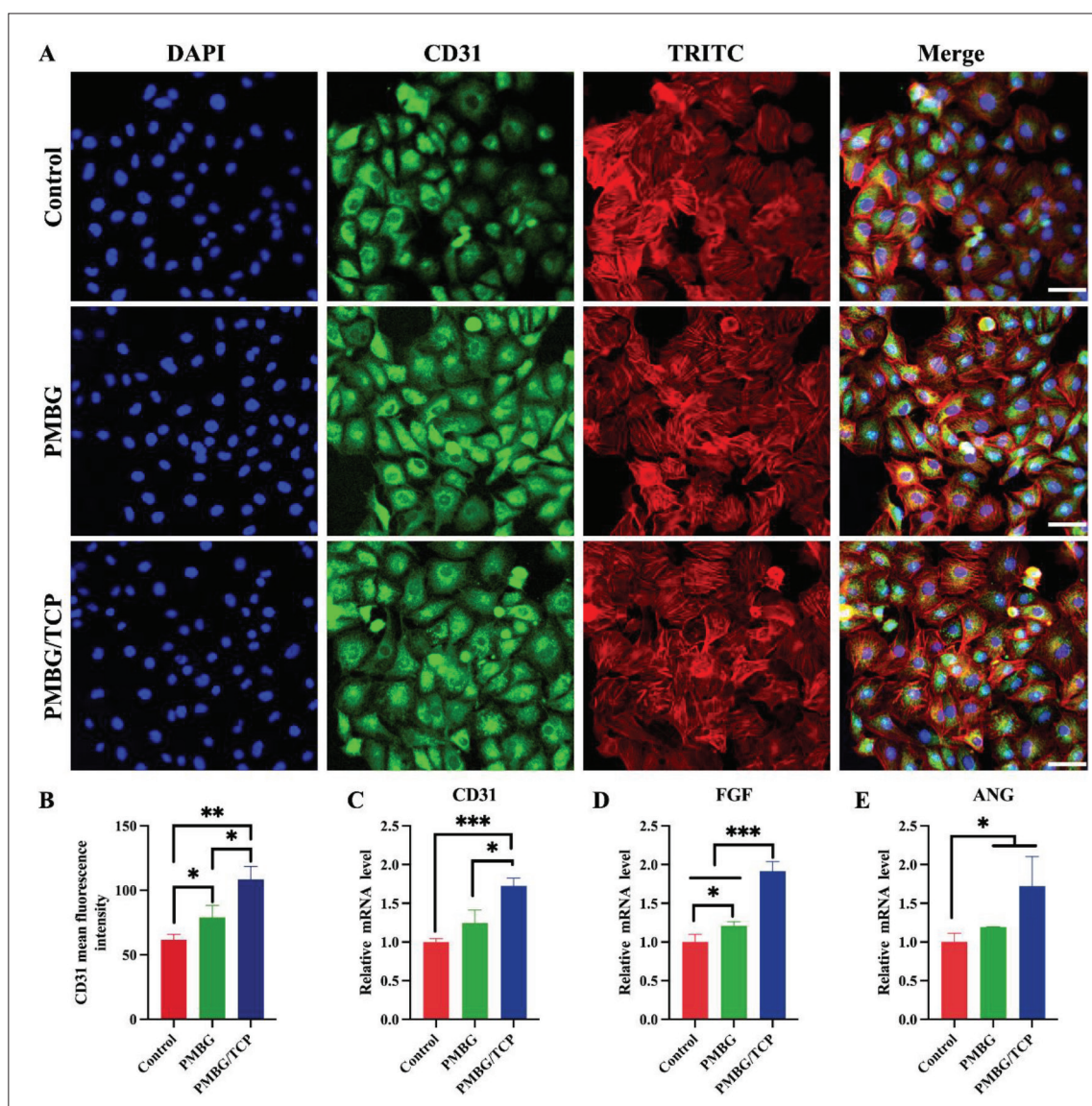
Figure 7. Effects of various prepared scaffolds on angiogenesis. (A, B) Immunofluorescence confocal images and quantitative analysis of the angiogenesis markers CD31 (scale bar = 50 μm). Angiogenesis gene expression of (C) *CD31*, (D) *FGF*, and (E) *ANG*.

points (Figure 8C and D). These results indicate that the PMBG/TCP scaffold successfully repaired critical-sized bone defects, and the PMBG/TCP scaffold group had a faster and better new bone fusion rate compared to the other groups.

Furthermore, H&E and Masson's trichrome staining were applied to investigate the effect of the prepared scaffolds on bone regeneration. As shown in Figure 9A and B, no inflammation or necrosis was observed in the stained sections of all groups after implantation. Moreover, new bone and fibrous tissue appeared in the PMBG scaffold group and the PMBG/TCP scaffold group, while the defect area in the control group was only partially filled

with scattered fibrous tissue. The PMBG/TCP scaffold group, due to the addition of TCP, showed superior bone regeneration ability compared to the PMBG scaffold group. Additionally, it could be observed that the PMBG/TCP scaffold filled the defect, and the surface pores of the scaffold were filled with newly formed mineralized bone. The newly formed bone tissue filled all corners of the scaffold and even extended to the entire defect area. Furthermore, more bone tissue growth promoted scaffold degradation.

It has been reported that silicon elements can promote vascular regeneration, which is crucial for bone regeneration[40,41]. Therefore, we further validated the ability
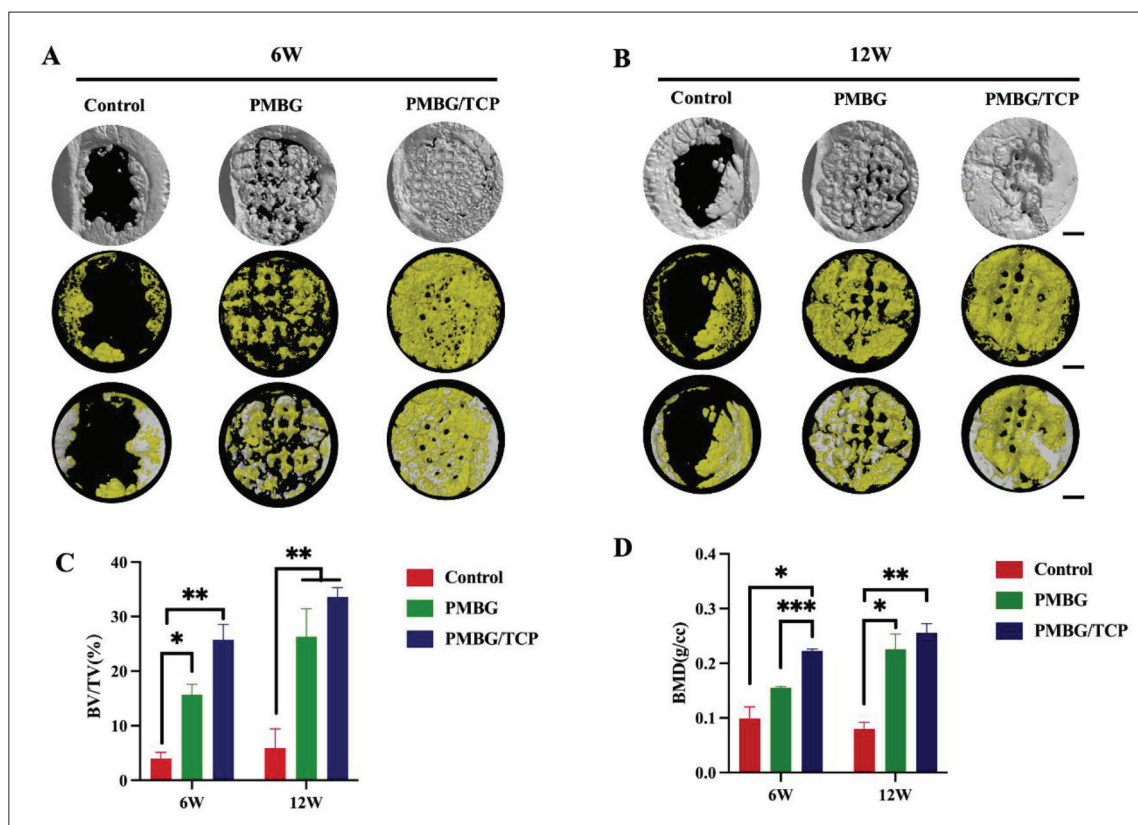
Figure 8. *In vivo* performance of various scaffolds for repairing bone defects. (A) 3D micro-CT reconstructed images of bone defect repair *in vivo* at 6 and 12 weeks, denoted by 6W and 12W in the figure, respectively. (B) Micro-CT images of the regenerative repair effect of implanted scaffolds *in vivo* (yellow indicates regenerated bone tissue; gray indicates scaffolds without degradation), including (C) BV/TV and (D) BMD. Scale bar = 1 mm.

of the PMBG/TCP scaffold to promote vascularized bone regeneration using immunofluorescence staining. CD31, a vascular endothelial cell marker, was used to immunostain tissue sections from each group at 6 weeks after surgery. As shown in Figure 9C, the expression of CD31 in the newly formed bone vessels in the PMBG scaffold group and the PMBG/TCP scaffold group was significantly stronger than that in the control group, with the PMBG/TCP scaffold group showing the strongest CD31 expression. This indicates that the PMBG/TCP scaffold has excellent ability to promote vascularization. In addition, the expression of osteocalcin (OCN), a bone cell marker, was significantly increased in the PMBG/TCP scaffold group compared to the other two groups (Figure 9B). These results confirm that the PMBG/TCP scaffold has excellent ability to promote vascularized bone regeneration *in vivo*, which is consistent with the *in vitro* experimental results.

4. Conclusion

In this study, we developed a dual-functionalized PMBG sol gel that enables ultrafast photo-crosslinking, and further incorporated nanosized TCP particles via 3D printing technology to prepare PMBG/TCP biphasic scaffolds. The photo-crosslinking PMBG/TCP printing process has addressed the complexity and lack of personalization of the traditional MBG preparation methods, while the introduction of rigid particles significantly improves the compressive strength of the scaffolds. The phosphate units are integrated into the bioactive glass network, thereby enhancing network connectivity and resisting rapid degradation. The released ions (SiO_4^{4-} and Ca^{2+}) further create a vascularized bone regeneration microenvironment, which is crucial for rapid bone regeneration. The development of this photo-crosslinking PMBG/TCP scaffold and its integration with innovative manufacturing technology provide a feasible approach for personalized and precise treatment of traditional bone repair materials. However, innovative artificial bone still faces several challenges in clinical translation, such as low product acceptance and difficult regulatory approval. In the future, with the development of materials science and the popularization of 3D printing technology, the innovative method developed in this study will be used to construct clinical artificial bone with excellent comprehensive properties.
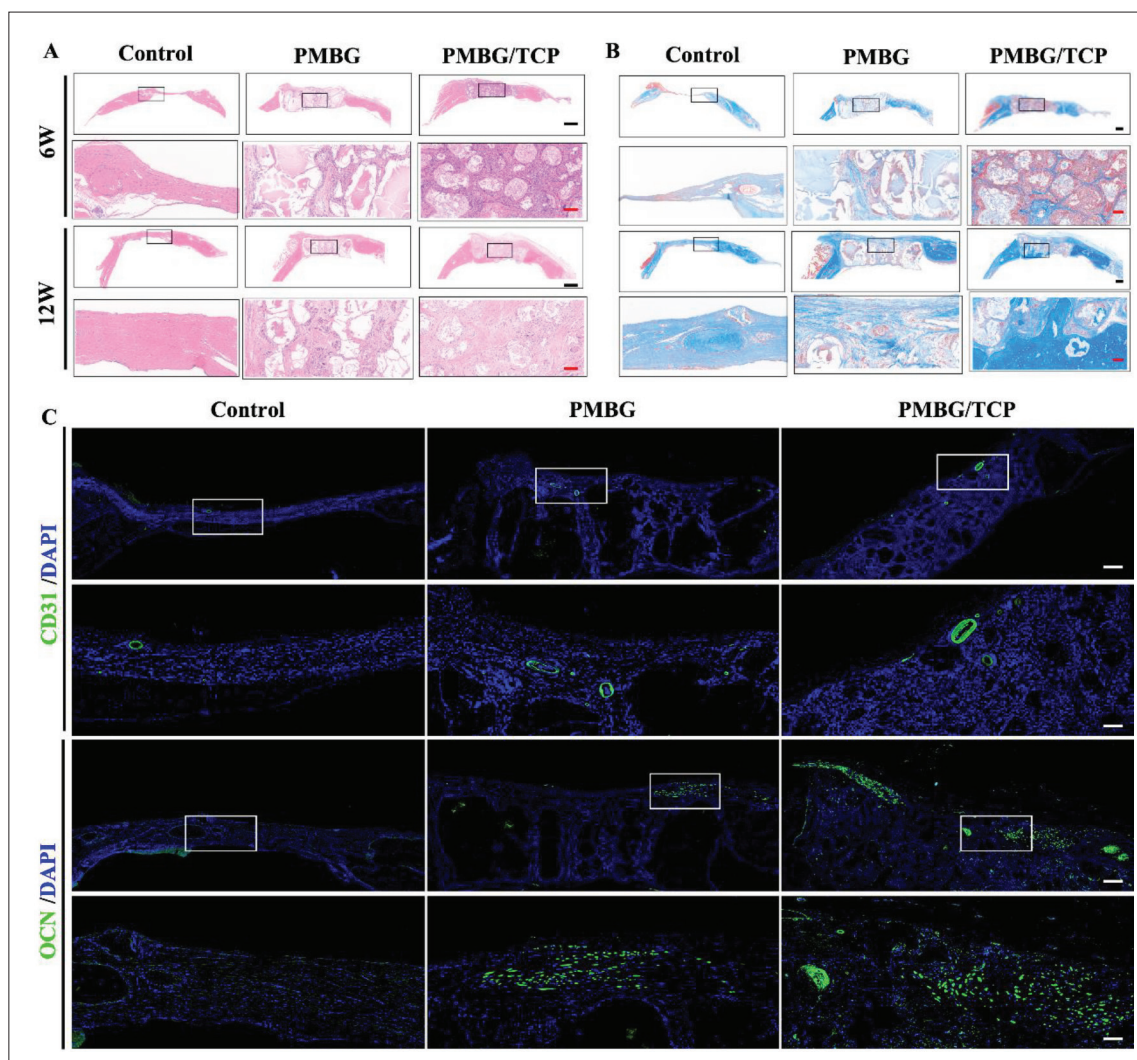
Figure 9. Histomorphometric assessment of bone regeneration at specific time intervals for each Implant. (A) H&E staining for each implantation *in vivo*. (B) Masson's trichrome staining for each implantation *in vivo*. (C) Immunofluorescence images of *in vivo* tissue angiogenesis marker CD31 and osteogenic marker OCN. Red scale bar = 100 μm, black scale bar = 1000 μm, and white scale bar = 100 μm.

Acknowledgments

Funding

Conflict of interest

The authors declare no conflict of interest.

Author contributions

Conceptualization: Changru Zhang, Ya Ren, Heyue Li
Formal analysis: Changru Zhang, Ya Ren,
Fund acquisition: Han Yang, Bin Cai
Project administration: Han Yang, Bin Cai
Visualization: Chengwei Wang, Liang Tang, Haoyi Niu
Writing – original draft: Changru Zhang, Ya Ren, Weiqing Kong, Yihao Liu, Heyue Li

Writing – review & editing: Changru Zhang, Ya Ren, Yihao Liu, Kerong Dai, Jinwu Wang

Ethics approval and consent to participate

The animal experiment in this study was approved by the Animal Research Committee of Ninth People's Hospital, Shanghai Jiao Tong University School of Medicine (License number: SH9H-2020-T269-4).

Consent for publication

Not applicable.

Availability of data

The data that support the findings of this study are available from the corresponding author upon reasonable request.

References

1. Petersen A, Princ A, Korus G, *et al.*, 2018, A biomaterial with a channel-like pore architecture induces endochondral healing of bone defects. *Nat Commun*, 9(1): 4430.

   https://doi.org/10.1038/s41467-018-06504-7

2. Okuchi Y, Reeves J, Ng SS, *et al.*, 2021, Wnt-modified materials mediate asymmetric stem cell division to direct human osteogenic tissue formation for bone repair. *Nat Mater*, 20(1): 108–118.

   https://doi.org/10.1038/s41563-020-0786-5

3. Salhotra A, Shah HN, Levi B, *et al.*, 2020, Mechanisms of bone development and repair. *Nat Rev Mol Cell Biol*, 21(11): 696–711.

   https://doi.org/10.1038/s41580-020-00279-w

4. Zhao R, Shang T, Yuan B, *et al.*, 2022, Osteoporotic bone recovery by a bamboo-structured bioceramic with controlled release of hydroxyapatite nanoparticles. *Bioact Mater*, 17: 379–393.

   https://doi.org/10.1016/j.bioactmat.2022.01.007

5. Hao J, Bai B, Ci Z, *et al.*, 2022, Large-sized bone defect repair by combining a decalcified bone matrix framework and bone regeneration units based on photo-crosslinkable osteogenic microgels. *Bioact Mater*, 14: 97–109.

   https://doi.org/10.1016/j.bioactmat.2021.12.013

6. Feng B, Zhang M, Qin C, *et al.*, 2023, 3D printing of conch-like scaffolds for guiding cell migration and directional bone growth. *Bioact Mater*, 22: 127–140.

   https://doi.org/10.1016/j.bioactmat.2022.09.014

7. Liu H, Du Y, St-Pierre J-P, *et al.*, 2020, Bioenergetic-active materials enhance tissue regeneration by modulating cellular metabolic state. *Sci Adv*, 6(13): eaay7608.

   https://doi.org/10.1126/sciadv.aay7608

8. Yu M, Du Y, Han Y, *et al.*, 2020, Biomimetic elastomeric bioactive siloxane-based hybrid nanofibrous scaffolds with miRNA activation: A joint physico-chemical-biological strategy for promoting bone regeneration. *Adv Funct Mater*, 30(4): 1906013.

   https://doi.org/10.1002/adfm.201906013

9. Chen Q, Yu S, Zhang D, *et al.*, 2019, Impact of antifouling PEG layer on the performance of functional peptides in regulating cell behaviors. *J Am Chem Soc*, 141(42): 16772–16780.

   https://doi.org/10.1021/jacs.9b07105

10. Zhang X, Chen X, Hong H, *et al.*, 2022, Decellularized extracellular matrix scaffolds: Recent trends and emerging strategies in tissue engineering. *Bioact Mater*, 10: 15–31.

    https://doi.org/10.1016/j.bioactmat.2021.09.014

11. Chen X, Wang M, Chen F, *et al.*, 2020, Correlations between macrophage polarization and osteoinduction of porous calcium phosphate ceramics. *Acta Biomater*, 103: 318–332.

    https://doi.org/10.1016/j.actbio.2019.12.019

12. Zhao F, Yang Z, Xiong H, *et al.*, 2023, A bioactive glass functional hydrogel enhances bone augmentation via synergistic angiogenesis, self-swelling and osteogenesis. *Bioact Mater*, 22: 201–210.

    https://doi.org/10.1016/j.bioactmat.2022.09.007

13. Aleman J, Kilic T, Mille LS, *et al.*, 2021, Microfluidic integration of regeneratable electrochemical affinity-based biosensors for continual monitoring of organ-on-a-chip devices. *Nat Protoc*, 16(5): 2564–2593.

    https://doi.org/10.1038/s41596-021-00511-7

14. Zhao H, Liang G, Liang W, *et al.*, 2020, In vitro and in vivo evaluation of the pH-neutral bioactive glass as high performance bone grafts. *Mater Sc Eng C*, 116: 111249.

    https://doi.org/10.1016/j.msec.2020.111249

15. Zhao F, Xie W, Zhang W, *et al.*, 2018, 3D printing nanoscale bioactive glass scaffolds enhance osteoblast migration and extramembranous osteogenesis through stimulating immunomodulation. *Adv Healthc Mater*, 7(16): e1800361.

    https://doi.org/10.1002/adhm.201800361

16. Zheng X, Zhang X, Wang Y, *et al.*, 2021, Hypoxia-mimicking 3D bioglass-nanoclay scaffolds promote endogenous bone regeneration. *Bioact Mater*, 6(10): 3485–3495.

    https://doi.org/10.1016/j.bioactmat.2021.03.011

17. Zhi W, Wang X, Sun D, *et al.*, 2022, Optimal regenerative repair of large segmental bone defect in a goat model with osteoinductive calcium phosphate bioceramic implants. *Bioact Mater*, 11: 240–253.

    https://doi.org/10.1016/j.bioactmat.2021.09.024

18. Koons GL, Diba Mand Mikos AG, 2020, Materials design for bone-tissue engineering. *Nat Rev Mater*, 5(8): 584–603.

    https://doi.org/10.1038/s41578-020-0204-2

19. Richter RF, Ahlfeld T, Gelinsky M, *et al.*, 2023, Composites consisting of calcium phosphate cements and mesoporous bioactive glasses as a 3D plottable drug delivery system. *Acta Biomater*, 156: 146–157.

 https://doi.org/10.1016/j.actbio.2022.01.034

20. Wu L, Pei X, Zhang B, *et al.*, 2023, 3D-printed HAp bone regeneration scaffolds enable nano-scale manipulation of cellular mechanotransduction signals. *Chem Eng J*, 455: 140699.

 https://doi.org/10.1016/j.cej.2022.140699

21. Autefage H, Allen F, Tang HM, *et al.*, 2019, Multiscale analyses reveal native-like lamellar bone repair and near perfect bone-contact with porous strontium-loaded bioactive glass. *Biomaterials*, 209: 152–162.

 https://doi.org/10.1016/j.biomaterials.2019.03.035

22. Zhang M, Zhai X, Ma T, *et al.*, 2023, Sequential therapy for bone regeneration by cerium oxide-reinforced 3D-printed bioactive glass scaffolds. *ACS Nano*, 17(5): 4433–4444.

 https://doi.org/10.1021/acsnano.2c09855

23. Li S, Zhang L, Liu C, *et al.*, 2023, Spontaneous immunomodulation and regulation of angiogenesis and osteogenesis by Sr/Cu-borosilicate glass (BSG) bone cement to repair critical bone defects. *Bioact Mater*, 23: 101–117.

 https://doi.org/10.1016/j.bioactmat.2022.10.021

24. Zhu H, Zheng K, Boccaccini AR, 2021, Multi-functional silica-based mesoporous materials for simultaneous delivery of biologically active ions and therapeutic biomolecules. *Acta Biomater*, 129: 1–17.

 https://doi.org/10.1016/j.actbio.2021.05.007

25. Zhu H, Monavari M, Zheng K, *et al.*, 2022, 3D bioprinting of multifunctional dynamic nanocomposite bioinks incorporating Cu-doped mesoporous bioactive glass nanoparticles for bone tissue engineering. *Small*, 18(12): e2104996.

 https://doi.org/10.1002/smll.202104996

26. Niu HY, Ma YF, Wu GY, *et al.*, 2021, Multicellularity-interweaved bone regeneration of BMP-2-loaded scaffold with orchestrated kinetics of resorption and osteogenesis (vol 216, 119216, 2019). *Biomaterials*, 216: 119216.

 https://doi.org/10.1016/j.biomaterials.2020.120376

27. Zhou Y, Wu C, Chang J, 2019, Bioceramics to regulate stem cells and their microenvironment for tissue regeneration. *Mater Today*, 24(C): 41–56.

 https://doi.org/10.1016/j.mattod.2018.07.016

28. Ma H, Feng C, Chang J, *et al.*, 2018, 3D-printed bioceramic scaffolds: From bone tissue engineering to tumor therapy. *Acta Biomater*, 79: 37–59.

 https://doi.org/10.1016/j.actbio.2018.08.026

29. Tang F, Li J, Xie W, *et al.*, 2021, Bioactive glass promotes the barrier functional behaviors of keratinocytes and improves the Re-epithelialization in wound healing in diabetic rats. *Bioact Mater*, 6(10): 3496–3506.

 https://doi.org/10.1016/j.bioactmat.2021.02.041

30. Schumacher M, Habibovic P, van Rijt S, 2021, Mesoporous bioactive glass composition effects on degradation and bioactivity. *Bioact Mater*, 6(7): 1921–1931.

 https://doi.org/10.1016/j.bioactmat.2020.12.007

31. Chai Y, Lin D, Ma Y, *et al.*, 2017, RhBMP-2 loaded MBG/PEGylated poly(glycerol sebacate) composite scaffolds for rapid bone regeneration. *J Mater Chem B*, 5(24): 4633–4647.

 https://doi.org/10.1039/c7tb00505a

32. Ding X, Shi J, Wei J, *et al.*, 2021, A biopolymer hydrogel electrostatically reinforced by amino-functionalized bioactive glass for accelerated bone regeneration. *Sci Adv*, 7(50): eabj7857.

 https://doi.org/10.1126/sciadv.abj7857

33. Lin D, Cai B, Wang L, *et al.*, 2021, A viscoelastic PEGylated poly(glycerol sebacate)-based bilayer scaffold for cartilage regeneration in full-thickness osteochondral defect (vol 253, 120095, 2020). *Biomaterials*, 253: 120095.

 https://doi.org/10.1016/j.biomaterials.2020.120618

34. Ma LL, Zhou YL, Zhang ZWB, *et al.*, 2020, Multifunctional bioactive Nd-Ca-Si glasses for fluorescence thermometry, photothermal therapy, and burn tissue repair. *Sci Adv*, 6(32): eabb1311.

 https://doi.org/10.1126/sciadv.abb1311

35. Liu Y, Ma Y, Zhang J, *et al.*, 2017, MBG-modified beta-TCP scaffold promotes mesenchymal stem cells adhesion and osteogenic differentiation via a FAK/MAPK signaling pathway. *ACS Appl Mater Interfaces*, 9(36): 30283–30296.

 https://doi.org/10.1021/acsami.7b02466

36. Zhou M, Li B, Li N, *et al.*, 2022, Regulation of Ca2+ for cancer cell apoptosis through photothermal conjugated nanoparticles. *ACS Appl Bio Mater*, 5(6): 2834–2842.

 https://doi.org/10.1021/acsabm.2c00236

37. Gu J, Zhang Q, Geng M, *et al.*, 2021, Construction of nanofibrous scaffolds with interconnected perfusable microchannel networks for engineering of vascularized bone tissue. *Bioact Mater*, 6(10): 3254–3268.

 https://doi.org/10.1016/j.bioactmat.2021.02.033

38. Zhang C, Li T, Yin S, *et al.*, 2022, Monocytes deposit migrasomes to promote embryonic angiogenesis. *Nat Cell Biol*, 24(12): 1726.

 https://doi.org/10.1038/s41556-022-01026-3

39. Wu J, Lu Z, Jiang D, *et al.*, 2021, Iterative tomography with digital adaptive optics permits hour-long intravital observation of 3D subcellular dynamics at millisecond scale. *Cell*, 184(12): 3318.

https://doi.org/10.1016/j.cell.2021.04.029

40. Ma W, Ma H, Qiu P, *et al.*, 2021, Sprayable beta-FeSi2 composite hydrogel for portable skin tumor treatment and wound healing. *Biomaterials*, 279: 121225.

https://doi.org/10.1016/j.biomaterials.2021.121225

41. Ma Y-X, Jiao K, Wan Q-Q, *et al.*, 2022, Silicified collagen scaffold induces semaphorin 3A secretion by sensory nerves to improve in-situ bone regeneration. *Bioact Mater*, 9: 475–490.

https://doi.org/10.1016/j.bioactmat.2021.07.016